Characterization of palladium/copper/ceria electrospun fibers for water–gas shift catalysis

William T. Gibbons [a], Tracy H. Liu [a], Karen J. Gaskell [b], Gregory S. Jackson [c,*]

[a] Department of Chemical Engineering, University of Maryland, College Park, MD 20742, USA
[b] Department of Chemistry and Biochemistry, University of Maryland, College Park, MD 20742, USA
[c] Department of Mechanical Engineering, University of Maryland, College Park, MD 20742, USA

ABSTRACT

Nano-fibers of palladium–copper (Pd/Cu) in ceria for water–gas-shift (WGS) catalysis were prepared by electrospinning solutions containing polyvinylpyrrolidone (PVP) and soluble salts of cerium, palladium, and copper in a water/ethanol co-solvent. Catalyst precursors were mixed in a single pot, electro-spun, and calcined to produce ceramic fibers with 88 wt% CeO_2, 2% Pd, and 10% Cu. Slowing the rate of polymer removal with controlled heating during calcining did not significantly change fiber diameters (~200 nm) but did lower the ceria crystallite to typically less than 10 nm and produce longer fibers that formed non-woven mats with structural integrity. The resulting catalyst materials were characterized for WGS activity by temperature-programmed and time-on-stream reactor tests. X-ray photoelectron spectroscopy, Raman spectroscopy, and transmission electron microscopy analysis indicated that for different precursor salts, much of the Cu and Pd are incorporated into the ceria lattice before testing. For the Pd/Cu/ceria nano-fiber catalysts, time-on-stream testing at 400 °C showed high WGS activity, that asymptotically decayed with time. Post-testing XPS and Raman spectroscopy indicated that reduced Pd and Cu segregate to the surface during time-on-stream testing, which lowers activity. Exposure to intermittent oxidizing environments, particularly with O_2, partially reverses the metal segregation and restores catalyst activity. Adding surfactant to the synthesis solution increases catalyst surface area without significantly improving activity or slowing its asymptotic decay, which suggests that activity is not limited strictly by surface area, but rather by metal/ceria interactions, for these catalysts.

© 2014 Elsevier B.V. All rights reserved.

1. Introduction

Water–gas-shift (WGS) catalytic reactors provide removal of CO and increased H_2 content from hydrocarbon reformate streams for H_2 production in fuel cell systems, coal gas processing, and other applications. The exothermic WGS reaction indicated in reaction R1 removes CO by reacting with excess H_2O in the reformate stream:

$$H_2O + CO \leftrightarrow CO_2 + H_2 + 41\,kJ/gmol\,(at\,300\,K). \tag{R1}$$
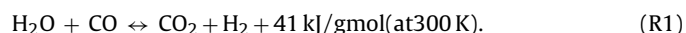
The WGS reaction is relatively fast in both the forward and reverse reaction over common Cu/Zn/Al catalysts at temperatures down to around 400 °C, and in sufficiently large reactors, (R1) approaches equilibrium such that CO concentrations reach mole fractions below 0.5% on a wet basis depending on the reformate. The Cu/Zn/Al catalysts, however, suffer from poor activity below 350 °C and irreversible loss of activity upon exposure to air at operating temperatures, which presents challenges for operability of these catalysts, particularly for H_2 purification in fuel cell applications [1].

The exothermic nature of (R1) suggests that more active catalysts can reach equilibrium at lower temperatures with lower CO concentrations. Efforts have developed more active ceria-based WGS catalysts, which can approach thermodynamic equilibrium at temperatures well below 400 °C and which have increased stability in oxidizing environments [2,3]. More active catalysts may reduce WGS reactor size and thereby their start-up times [4,5].

Significant research efforts in recent years on ceria-based WGS catalysts have shown that these catalysts can provide higher activity and improved resistance to deactivation from start-stop cycles. Ceria-based supports with active metal catalysts (Pt, Au, Pd, Cu, and their alloys) have been explored broadly [6–20] and have shown promise for use in compact reactors for hydrocarbon

fuel processors for fuel cell systems [21]. The WGS reaction mechanism on the ceria-based catalysts remains a matter of debate over the rate-limiting step in the reaction process [3], although it is clear that strong interactions between the ceria and metal catalyst play a key role in activity [15,22,23]. The debate concerns the role in limiting reaction rates of decomposition of observed intermediate surface species, such as formates and/or carbonates, and the role of the support redox cycle for water dissociation [24–27]. Different conclusions have been drawn which may in part be due to different test conditions and different interactions between the ceria-support and the catalytic metal species. For example, ceria-supported metal catalysts and ceria catalysts with metal incorporation into the ceria lattice may have differrent rate limiting steps in the WGS reaction [28]. All the same, ceria-based catalysts with either supported or impregnated metals show a tendency to slowly lose activity in time-on-stream studies [20], and ongoing efforts are exploring how to understand and control the metal–ceria structures and interactions to improve the stability of the WGS activity [29,30]. Because ceria-based catalysts show high activity with relatively low transition metal loadings, they are worthy of continued exploration and development.

Approaches to synthesis of ceria-based WGS catalysts include incipient wetness addition of metals on ceria supports and co-precipitation of metals and ceria from solution. Incipient wetness techniques and related sequential deposition methods tend to produce distinct metal/metal oxides supported on ceria. On the other hand, co-precipitation methods with oxophilic metals like Cu or even Pd can produce strong metal–ceria interactions, which can include cation incorporation into the ceria lattice for Cu [13] and/or Pd [31]. However, even for Cu-ceria catalysts formed by co-precipitation, studies have shown that these catalysts are prone to partially reversible deactivation due to the formation of low-activity metal species on the surface in the reducing WGS environment [32]. Other recent studies showed that WGS activity of co-precipitated Cu-ceria catalysts increased with oxidized Cu content [33] and that activity was best maintained with very strong interactions between the Cu and the ceria at the catalyst surface [34].

Synthesis of highly active ceria-based WGS catalysts can produce strong metal–ceria interactions by incorporating the metal cation into the ceria-lattice. Co-precipitation or a similar method in which the metal and ceria precursors are intimately mixed is often more desirable than metal deposition processes onto an already synthesized ceria support [13]. Electrospinning of mixed ceria/metal precursors provides one such technique that allows for simple synthesis of intimately mixed catalytically active material. Electrospinning has been used widely to produce polymer-based fibers, and more recently explored as a method for producing ceria-based or other oxide fibers [35–41]. This technique provides the basis for a simple route to catalytically active metal/metal–oxide materials, though few ceria-based catalysts have been produced via electrospinning to date [42,43]. Electrospinning of an appropriate solution as described in this study can achieve intimate mixing of active metals like Cu and Pd with CeO$_2$ while producing high-surface-area structures with well-dispersed nano-scale grains for promoting catalytic activity.

For this study, a series of ceria-based catalysts containing Pd and/or Cu were produced via electrospinning. Since the Pd/Cu system has been characterized by others and shown to have high activity under WGS and oxygen-assisted WGS conditions [31,44,45], the primary composition of metals was held at 2/10 wt% Pd/Cu as a model system for the exploration of the electrospun ceria-based WGS catalysts. The Pd/Cu system was compared to the single metal equivalents with 2 wt% Pd or 10 wt% Cu to explore the synergistic effects between the Pd and Cu that have been observed in the previous studies of ceria-based catalysts.

This study investigates how adjustments in the electrospinning process can influence the structure and activity of the Pd/Cu/ceria nano-fiber catalysts. Changes in the structure of the ceria-based nanofibers can be manipulated through changes in the precursor salts and/or the calcining process. Such structural changes may impact the WGS catalyst performance including the rate of reversible deactivation as well as near steady-state performance. This study also explores the transient WGS activity (without O$_2$ assistance) of the electrospun Pd/Cu/ceria catalysts as well as their reactivation due to exposure to oxidizing environments in order to shed light on the relationship between catalyst structure (in terms of metal/ceria interactions) and activity. Examination of the catalyst structure and surface composition before and after testing in the reducing WGS environment as well as after exposure to heated oxidizing environments provides a basis for describing the dynamic nature of the metal–ceria interactions and their impact on catalyst stability. In general, the study presents the potential for electrospun catalysts to provide a simple one-pot synthesis approach to developing nano-crystalline ceria-based catalysts with good catalytic activity and macro-scale handling properties.

2. Experimental methods

2.1. Catalyst fabrication

Catalysts were prepared via a one-pot synthesis based on electrospinning a salt solution and subsequent calcining. For a typical synthesis, ~12 mL of spinning solution was prepared by adding 1.94 g Ce(NO$_3$)$_3$·6H$_2$O, 0.044 g Pd(NO$_3$)$_2$·2H$_2$O, and some amount of a hydrated copper salt to a solution consisting of 6.60 g ethanol and 6.00 g water (60 vol% ethanol). Most mixtures were designed to produce a catalyst consisting of 2 wt% Pd, 10 wt% Cu, 88 wt% CeO$_2$ when the Pd and Cu are fully reduced. As discussed in the results, the metals were likely fully oxidized after calcining resulting in an actual composition of 2.2 wt% PdO, 12.2% CuO, and 85.6% CeO$_2$. Furthermore, as discussed below, characterization suggests that after calcination, the Pd and Cu are incorporated into the ceria lattice and then undergo some amount of phase separation during reduction in the reducing WGS environment. As such, defining the weight fractions is problematic and the catalysts will simply be referred to as 2/10 wt% Pd/Cu ceria-based catalysts. To compare with the Pd/Cu catalyst system, two single metal catalysts were also made: (1) with the same Pd to CeO$_2$ loading and no Cu and (2) with the same Cu (from an acetate precursor) to CeO$_2$ loading and no Pd.

Different copper salt hydrates were used in this study. Their respective amounts added to the solution to achieve the 10 wt% Cu in the final catalyst were 0.31 g for Cu(NO$_3$)$_2$·2H$_2$O, 0.30 g for Cu(CH$_3$COO)$_2$·H$_2$O, or 0.23 g for CuCl$_2$·2H$_2$O. After stirring at room temperature until dissolution was achieved, 1.44 g of granular polyvinylpyrrolidone (PVP with average *MW* of 1.3×10^6) was added and stirred into the solution overnight to produce a homogenous, viscous solution. For some catalyst samples, 0.2 g or 0.4 g of the surfactant Pluronic L-61 was added with the PVP. The surfactant addition reduced the solution surface tension and increased calcined fiber porosity due to the formation of micelles and voids in the fibers during the polymer removal process.

The final solution was electrospun in a 1.0 kV cm^{-1} electric field at a flow rate of 1 mL h^{-1} onto a rotating wire drum collector. The electric field was produced using two high voltage power supplies. The needle (or spinneret) was maintained at −20 kV and the collector was maintained at +2 kV to improve fiber collection efficiency and avoid deposition of fibers on surrounding surfaces [46]. The tip-to-collector distance was fixed at 22 cm to produce the desired 1.0 kV cm^{-1} electric field. The needle was cleaned every 15–20 min during spinning to avoid clogging.

For polymer removal and calcining of the original electrospun material, thermogravimetric analysis (TGA) was carried out in a CAHN 2131 TGA. Samples (10 ± 0.5 mg before polymer removal) were exposed to air at a flow rate of 100 standard cm^3 min^{-1} in the TGA, where they were heated slowly at variable heating rates in order to explore the effects of polymer oxidation process on the nanofiber/catalyst structures. The highly exothermic nature of the polymer removal (oxidation) process caused relatively high weight loss rates and significant temperature rise in a "rapid" heating process ($2\,°C$ min^{-1} in air to $550\,°C$ for 3 h). To reduce the rate of weight loss and the associated temperature rise, a more 'gentle' heating process at $0.1\,°C$ min^{-1} between 150 and $250\,°C$ was used to assess the role of calcination and the associated rate of polymer burnout on the fiber properties and resulting catalytic behavior. After polymer removal and calcination, the catalyst was loaded into a quartz reactor for activity and stability testing.

2.2. Catalyst material characterization

The electrospun fiber catalysts were characterized using an array of analytical techniques both before and after testing. Calcined fibers were characterized by X-ray diffraction (XRD) patterns obtained on a Bruker C2 Discover (Parallel Beam) General Area Diffraction Detection (GADDS) system with a Bruker ACS Hi-Star detector. Monochromatic Cu Kα radiation (40 KV and 40 mA) was used as the X-ray source. Approximately 10 mg of each fiber sample was pressed on to a glass slide for analysis and oscillated on the x–y axes during data collecting. Due to the equipment, XRD and other ex situ measurements were done after the catalyst was exposed to ambient air and thus highly oxophilic surfaces like ceria and segregated Cu-rich phases will undergo surface oxidation. This will not significantly impact the bulk-sensitive XRD, but it will impact surface-sensitive XPS and Raman measurements.

A Horiba LabRAM ARAMIS Raman spectrometer with a CCD detector used a diode pumped solid state laser (532 nm) and a grating of 600 grooves/mm to record Raman spectra for fresh as prepared catalyst and for catalyst post-testing and after re-oxidation. The spectra were collected by rastering the laser over a 15 μm $\times$ 15 μm spot size with a laser power of 29 μW measured at the sample. Catalyst samples were exposed to the laser for a total of 2 min (12 scans, 10 s per scan). The instrument grating was calibrated with a two-point calibration using a Si calibration standard (at wavenumbers of 0 cm^{-1} and 520.7 cm^{-1}).

In addition, X-ray photoelectron spectroscopy (XPS) was used to assess the catalyst surface composition before and after testing as well as after catalyst reactivation with exposure to O_2. XPS data were collected on a Kratos Axis 165 X-ray photoelectron spectrometer operating in hybrid mode using monochromatic Al Kα (1486.7 eV) X-rays. Survey and high-resolution spectra were collected with pass energies of 160 and 20 eV respectively. Charge neutralization was required to minimize charge build-up, and the pressure of the instrument was 5×10^{-8} Torr or better throughout data collection. Peak fittings for the Cu 2p, Pd 3d, Ce 3d, and O 1s spectra were done using Casa XPS software, employing peaks with a 30% Lorentzian and 70% Gaussian peak shape, but in this paper, only the Cu 2p and Pd 3d spectra are presented. Overlapping peaks in the Cu 2p$_{3/2}$ spectra present challenges to peak fitting, and thus it was important to establish a set approach to peak fitting. In this study, the Cu 2p$_{3/2}$ spectra were fit by constraining the two satellite peak separations associated with Cu^{2+} in CuO to be 6.4 and 9.3 eV from the main CuO peak at a binding energy (BE) of 934.2 eV. Additionally, the full width half maximum values (FWHM) of each CuO peak were fixed at 2.5, 3.1, 3.1 eV respectively, and the area of the main CuO peak was set to have an area ratio of 1.35 times the area of the combined satellite peaks.

N_2 adsorption provided an estimate for the fiber catalyst surface area. Samples were degassed by heating at $10\,°C$ min^{-1} to $90\,°C$ under vacuum, holding at $90\,°C$ for 1.0 h, and then heating at $10\,°C$ min^{-1} to $300\,°C$ for 3.0 h. After backfilling with N_2, samples were transferred from the degas port to the analysis port of the Micromeretics ASAP 2020 porosimeter. An 80-point N_2 adsorption/desorption isotherm was recorded. From the adsorption isotherm, BET surface areas were reported, and comparison of the adsorption and desorption isotherm branches indicate the presence (or lack) of microporosity within the fibers.

Fiber samples were examined in a Hitachi S-3400 Variable Pressure SEM with an accelerating voltage of 5 kV and a working distance of 10 mm. A column pressure of 100 Pa was set to reduce the effect of sample charging, which is especially pronounced, even for thin layers of the material, due to the insulating properties of the ceria-based fibers. Fiber samples were also prepared for TEM by sonicating a 2 mg sample of the catalyst in 2 mL anhydrous ethanol for 10 min before transferring the fiber solution to a Nickel TEM grid via pipette. After solvent evaporation, samples were loaded into a JEOL 2100 FEG-TEM for imaging. Particle size distributions were estimated using ImageJ image analysis software by measuring a random selection of at least 30 distinct particles. ImageJ software was also used to measure the plane spacings present in a sample of fresh catalyst examined via HRTEM. Measured plane spacings were compared to known values for CeO_2, CuO, and PdO.

2.3. Catalyst activity testing

Each tested catalyst sample was loaded into a quartz reactor (6.75 mm ID) between two plugs of quartz wool to yield a small packed bed reactor. Quartz sand upstream (5 g) and downstream (5 g) of the catalyst bed ensured well-mixed and thermally equilibrated flow through the catalyst bed. The mass of each catalyst sample was maintained at 50 ± 1 mg, and the bed height of each sample was fixed at 4 ± 0.2 mm. A Eurotherm 91P PID controller controlled the sample temperature, which was measured by a K-type thermocouple fixed at the leading (upstream) edge of the catalyst bed. The furnace temperature was maintained at $55\,°C$ before a testing cycle to avoid water condensation in the catalyst bed. 40 standard cm^3 min^{-1} of 5.5% CO (CP grade, Airgas) in Argon (UHP, Airgas), controlled by Brooks 5850 series mass flow controllers, flowed though a temperature controlled humidity bottle (Fuel Cell Technologies), maintained at $46\,°C$ to produce a WGS feed mixture containing 5% CO, 10% H_2O, and 85% Ar. Upon stabilizing the flow conditions at very close to 1 bar total pressure, the furnace temperature was ramped from 55 to $400\,°C$ at a rate of $2\,°C$ min^{-1}. All lines downstream of the humidity bottle were maintained above $60\,°C$ to prevent condensation, and water was removed from the reactor effluent through a Nafion membrane dryer (Permapure) with counter-flow dry air pulling the moisture from the effluent. The dried reactor effluent was analyzed by a Varian CP-4900 micro GC fitted with a PPU column (CO_2 analysis) and a MS5 column (H_2/CO analysis). Each column fed an independent thermal conductivity detector.

The temperature ramp with the constant feed mixture flowing through the catalyst bed provided a temperature programmed surface reaction (TPSR) characterization. In all TPSR tests, the CO_2 and H_2 effluent concentrations diverged (with CO_2 always in excess) as the catalyst bed temperature approached $100\,°C$. Prior to the activity testing, each catalyst was calcined at $550\,°C$ in air for 3 h before cooling to room temperature in air, and thus each catalyst component is assumed to be fully oxidized a (based on the following oxidation states Cu^{2+}O, Pd^{2+}O, and CeO$_2$). The difference between the H_2 and CO_2 concentrations in the effluent during the temperature ramp is likely due to CO reduction of the oxidized metals, including some CeO_2. This difference between product H_2 and
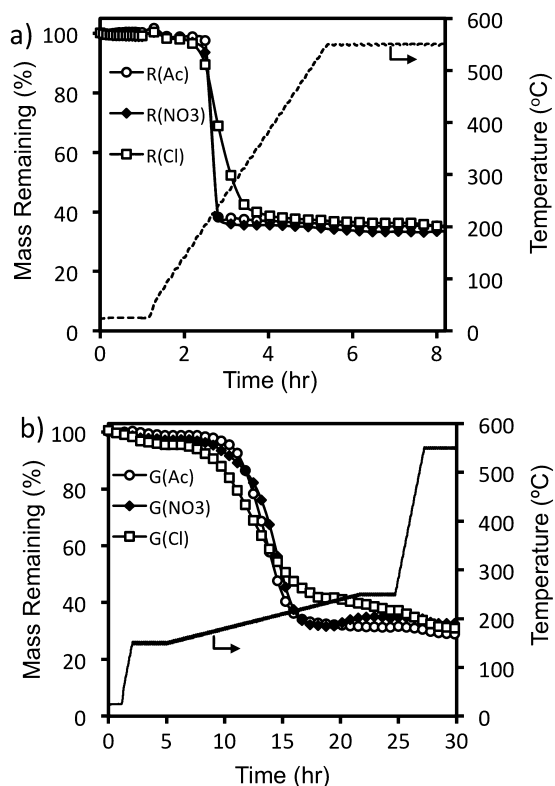
Fig. 1. Thermogravimetric analysis data with calcination temperature profiles for electrospun fibers (ceria with 2 wt% Pd and 10 wt% Cu) heated in air for polymer removal by oxidation (a) during rapid heating at 2 °C min^{-1} to 550 °C and (b) during gentle heating with indicated profile to 550 °C. All electrospun fibers used Ce(NO$_3$)$_3$·6H$_2$O and Pd(NO$_3$)$_2$·2H$_2$O as the CeO$_2$ and Pd sources respectively, and various precursor Cu salts were used as indicated in the labels.

CO$_2$ concentrations during the temperature ramp provided an estimate of the accessible oxygen from each catalyst. After the catalyst bed temperature reached 400 °C, time-on-stream tests monitored durability of WGS activity for each catalyst for at least 60 h at 400 °C.

3. Results and discussion

3.1. Impact of calcination

Polymer removal and calcining conditions for the ceria-based electrospun fibers were initially derived from those reported in literature for the production of various inorganic electrospun fiber materials using PVP or similar polymers dissolved using water/alcohol solvent systems. Most authors report a solvent removal or drying step followed by a heating step in which the polymer is decomposed in air [40–42,47–50]. Reported heating rates vary widely from 0.5 to 5.0 °C min^{-1}. Initially, the PVP removal and calcination step was performed by 'rapid' heating of the as-spun samples at 2 °C min^{-1} in air to 550 °C and holding there for 3 h. This 'rapid' polymer removal and calcination process is denoted throughout this text in the sample naming as 'R(X)' where X indicates the Cu precursor – 'Ac' for acetate, 'Cl' for chloride, and 'NO$_3$' for nitrate. Samples of fibers produced using different copper precursors were subjected to the rapid polymer removal and calcination in air, as shown in the TGA data in Fig. 1a. For the rapid heating, fibers spun with copper acetate and nitrate salts undergo the most rapid change in mass with rapid polymer oxidation occurring between 205 and 210 °C.

The rapidly heated samples produced relatively short, brittle fibers, which formed a fragile fiber mat (as shown in Fig. 2a) that readily crumbled into a powder-like substance. The short, brittle

fibers are the result of the rapid exothermic reaction causing fast sintering and fracturing in an environment similar to combustion synthesis [51]. These results are consistent with those of Pontelli et al. who produced Cu–CeO$_2$ fibers for methane oxidation from both PVP/cerium acetylacetonate and PVP/cerium nitrate solutions and found that the nitrate-based synthesis produced more fragmented fibers than the acetylacetonate synthesis [42]. In the present study, fibers produced using the copper chloride (R(Cl)) showed a much slower mass loss than the R(Ac) and R(NO$_3$) samples as shown in Fig. 1a. Although the R(Cl) fibers showed a similar total mass loss, it occurred over the course of approximately 2 h likely because chloride ions suppress free radical formation and thus the rate of polymer oxidation.

In order to produce a more structurally robust mat of ceramic fibers, a gentler polymer removal step (denoted 'G(X)' in sample naming where X indicates the Cu salt anion) was implemented with a reduced heating rate of 0.1 °C min^{-1} between 150 and 250 °C in order to slow decomposition of the polymer and metal salts. The reduced heating rate eliminated the thermal runaway and rapid temperature rise during polymer removal. TGA results for this gentle polymer removal in Fig. 1b provide evidence that the G(Ac) and G(NO$_3$) samples experienced the same mass loss over a period of 10 h as compared to the R(Ac) and R(NO$_3$) samples over 15 min. Again, the 'gentle' polymer removal from the copper chloride sample G(Cl) shows slower PVP decomposition than the G(Ac) and G(NO$_3$) samples with the total mass loss occurring over 20 h for the G(Cl) sample and only 5 h for the G(Ac) and G(NO$_3$) samples.

All of the G(X) samples showed non-woven mat morphology with significant structural robustness as illustrated in the photo of Fig. 2b. The 'gentle' process produces longer fibers with improved ductility (likely due to smaller grains from lower local sintering temperatures). SEM images in Fig. 2c and d comparing the R(Ac) and G(Ac) fibers show similar fiber diameters, but the integrated structure illustrated in Fig. 2a and b are dramatically different. The slower polymer removal process routinely formed a single electrospun ceramic-fiber mat. These results indicate that the polymer removal step must be tuned for electrospun ceramics in order to achieve a desired integrated structure at larger scales.

To gain further insight into the differences of the R(X) and G(X) fibers, samples spun from the same solution with the rapid and gentle calcining methods were examined with XRD before and after activity testing. The XRD patterns for the various Cu precursors are shown in Fig. 3 with an expanded inset showing the region between the (2 0 0) and (2 2 0) CeO$_2$ peaks (2θ from 34° to 46°) where many Pd and Cu oxide and metallic peaks reside. Both the R(X) (Fig. 3a) and G(X) (Fig. 3b) samples have broad peaks indicating ceria crystallite sizes less than 15 nm. Reitveld refinement was used to examine crystallite size with the results provided in Table 1 for fresh untested samples. The rapidly calcined samples produce larger CeO$_2$ crystallites for the same Cu precursors with the average around 13 nm for the fresh R(X) catalysts and around 9 nm for the fresh G(X) samples. This correlates with the increased brittleness of the R(X) samples and the higher sintering temperatures with the rapid oxidation during calcining. The samples tend to show some increases in crystallite domains due to extended testing (>60 h) in WGS environments at 400 °C, but the growth is not consistent nor substantial as shown in Table 1 to suggest that ceria sintering is significant at these temperatures. In summary, the exothermic oxidation during the PVP removal produces CeO$_2$ nano-crystalline fibers, which are relatively resistant to sintering at WGS operating temperatures.

The untested or 'fresh' samples after calcination show no evidence of reduced metal peaks in the XRD as shown in the inserts in Fig. 3a and b. The diffraction patterns of the untested samples are dominated by CeO$_2$ peaks with varying amounts of CuO present. The G(Cl) catalyst shows the most intense CuO peaks, which
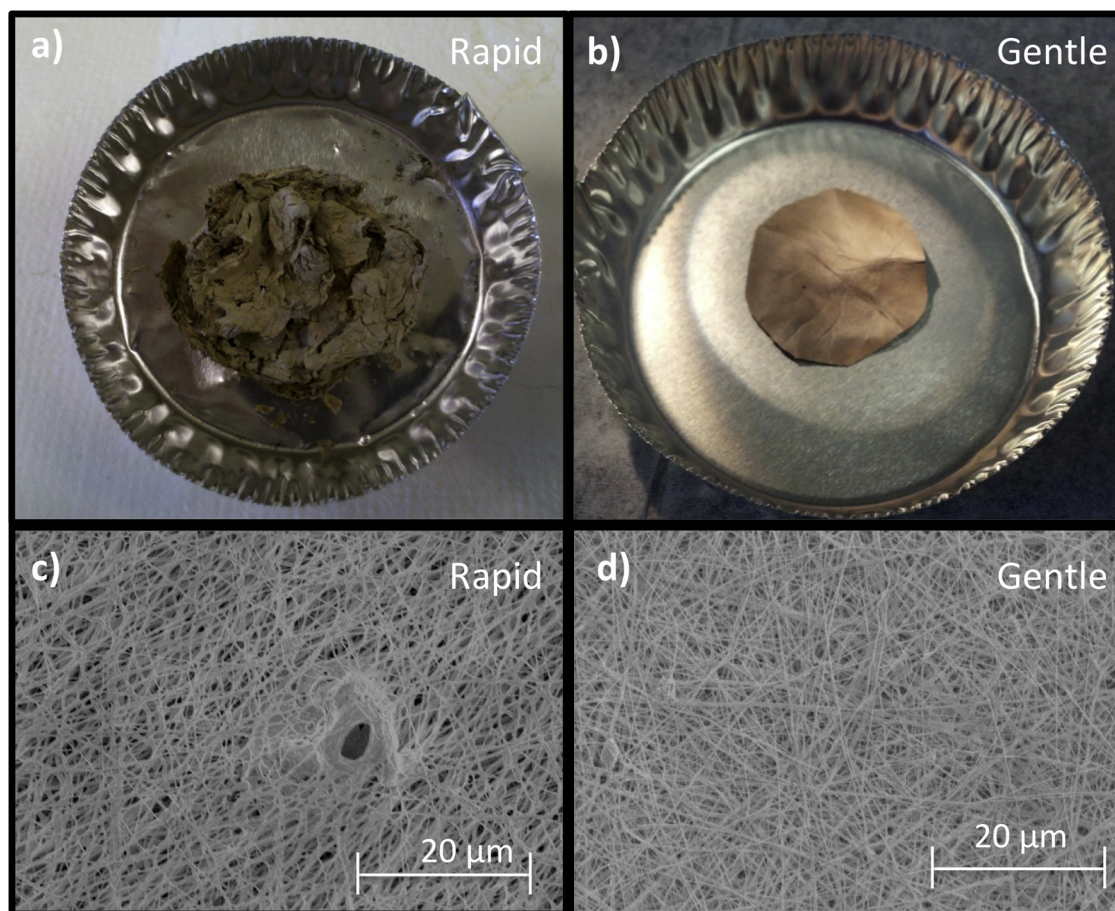
Fig. 2. Images showing electrospun catalyst material structure (∼50 mg) for the following conditions (a) 'rapid' heating at 2 K/min to 550 °C with copper acetate precursor and (b) 'gentle' heating as shown in Fig. 1a with copper acetate precursor. Samples of rapidly calcined fibers (c) and gently calcined fibers (d) are examined by SEM. Importantly, though the macroscopic structure of the spun fibers differs based on polymer removal method, the fiber structure is very similar on the micron-scale.

indicates that the $CuCl_2$ precursor in conjunction with the slower and cooler gentle calcination enhances Cu phase segregation relative to the other Cu salts. The less intense and broader CuO peaks for the other untested catalysts demonstrates smaller CuO crystallites associated with phase segregation.

While it is clear that there is some segregation of CuO in the untested catalysts, Reitveld analysis was used to analyze the lattice parameter for the catalysts with the various Cu precursors in order to explore how it might be influenced by possible Cu and Pd incorporation. Previous characterization of ceria catalysts with Cu-only incorporation have suggested that Cu impregnation does not greatly influence the ceria lattice parameter [3]. Competing effects are at play when doping the ceria fluorite lattice with the divalent Cu^{2+} and Pd^{2+} cations. The smaller ionic radii of both the Cu^{2+} and Pd^{2+} may suggest that doping would lower the lattice parameter, but the increased vacancies and lattice distortion due to doping can increase the lattice parameter. Table 1 provides lattice parameters for the various Pd–Cu fresh catalysts and their comparison with similarly prepared pure ceria fibers. The analysis does not reveal a clear trend as to the impact of any Cu or Pd incorporation into the catalyst, but the gently-calcined catalyst with the $CuCl_2$ precursor (G(Cl)) shows a significantly larger lattice parameter suggesting that this catalyst may have higher vacancy concentrations perhaps due to Cl^- incorporation or some other factor. Raman spectroscopy of the G(Cl) catalyst (not presented here) showed a significantly larger secondary peak attributed to ceria vacancies than the other catalysts, which further suggested the possibility of Cl^- in the ceria lattice. It should be noted that this catalyst showed exceptionally poor catalyst activity as discussed below.

Fig. 3a and b also shows the XRD analysis of samples tested for 60 h in WGS conditions at 400 °C. The samples demonstrate varying amounts of reduced copper species (Cu^0 and Cu^+, e.g., Cu_2O). The

Table 1
Lattice parameters and ceria crystallite sizes before and after testing for several different ceria-based catalysts prepared with various copper precursor salts.

Catalyst	Lattice parameter (with uncertainty) in nm		CeO_2 domain size (with uncertainty) in nm	
	Fresh	Tested	Fresh	Tested
G(Ac)	5.4151 (0.0017)	5.4171 (0.0020)	11.7 (0.5)	10.8 (0.5)
R(Ac)	5.4146 (0.0015)	5.4153 (0.0013)	13.7 (0.6)	17.2 (0.2)
G(Cl)	5.4207 (0.0031)	5.4196 (0.0021)	7.0 (0.3)	9.8 (0.4)
R(Cl)	5.4160 (0.0014)	5.4171 (0.0014)	14.9 (0.7)	13.5 (0.5)
G(NO$_3$)	5.4176 (0.0035)	5.4158 (0.0028)	7.3 (0.4)	9.3 (0.5)
R(NO$_3$)	5.4142 (0.0019)	5.4150 (0.0015)	9.7 (0.4)	12.7 (0.5)
CeO$_2$(ref)	5.4162 (0.0012)		14.0 (0.5)	
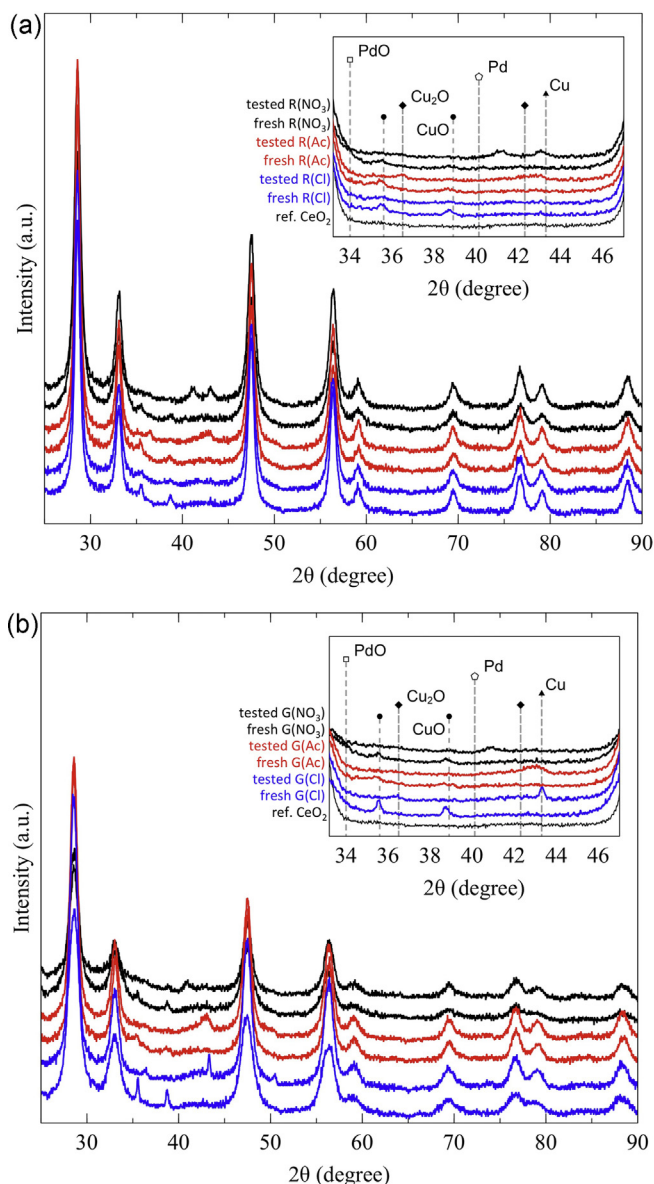
Fig. 3. XRD spectra for electrospun ceria fiber catalysts with 2 wt% Pd and 10 wt% Cu comparing results for different Cu precursors as calcined ('fresh') and after 60 h of WGS catalysis at 400 °C ('tested'). Samples include fiber catalyst subjected to (a rapid calcination as in Fig. 1a and b) gentle calcination as in Fig. 1b. All unlabeled peaks are associated with the fluorite oxide structure of CeO_2. Expanded region between 2θ of 34° and 46° provides information for Cu and Pd species as indicated by the labeled peak location.

lowest activity G(Cl) catalysts have the most intense peaks corresponding to fully and partially reduced Cu. These results suggest that surface CuO is readily reduced into pure Cu crystallites more so than Cu initially incorporated into the ceria lattice as observed in previously published work on Cu-impregnated ceria catalysts [3]. No clear evidence of Pd reduction is observed in the XRD, but this may be due to the low percentage of Pd in the catalyst. However, for both acetate and nitrate samples after testing, a broad peak at 2θ of 43°, which is at reduced angle of the pure Cu(1 1 1) peak, suggests the possibility of CuPd alloy domains with larger lattice parameters than pure Cu. The peaks at 2θ of 43° are not adequately resolved to make any claims regarding alloy composition. The impact of the phase segregation and reduced metal particle growth during testing as indicated by the XRD is discussed below in combination with the time-on-stream testing results.

The Reitveld analysis of the tested catalysts in Table 1 shows that in general the lattice parameter tends to grow with the testing in the reducing WGS environment and the associated metal segregation. Only the low activity G(Cl) untested catalyst remains with a lattice parameter outside (larger than) the region of confidence for the pure ceria lattice parameter. For most of the catalysts, testing in the WGS environments tends to increase crystallite domain size but only slightly. In general, XRD measurements have limited value in assessing the nature of the Pd-and/or Cu–ceria interactions other than to show segregated phases of reduced and oxidized metal.

To support the XRD, analysis of HRTEM images of the untested G(Ac) sample via ImageJ offer additional insight as to the ceria crystallite structure and composition. After measuring the plane spacings of non-overlapping particles at the regions of interest indicated in Fig. 4 the predominant plane spacings of all the particles measured indicate a CeO_2 phase. The HRTEM images provide no evidence to indicate the presence of particles of PdO or CuO, suggesting that the Pd and Cu after fabrication primarily reside as ionic species in the CeO_2 lattice. These results are in agreement with other references concerning Cu and/or Pd in CeO_2 formed by co-precipitation methods [3,28].

3.2. Role of catalyst composition

The activity testing of the catalysts was carried out by an initial heating in flowing reactants, which served as a temperature-programmed surface reaction (TPSR), and subsequent long-term time-on-stream testing at a constant 400 °C. The initial TPSR showed CO_2 production peaks between 65 and 200 °C without simultaneous H_2 production. Fig. 5 illustrates the low-temperature CO_2 production by comparing the CO_2 and H_2 production for a 2/10 wt% Pd/Cu catalyst while heating at 2 °C min^{-1} in 5% CO, 10% H_2O, and balance Ar. This low-temperature CO_2 production without H_2 production has been observed in another recent study with Cu-impregnated ceria catalysts for WGS TPSR [13]. The excess CO_2 at low-temperatures comes from CO oxidation by oxygen released by the reduction of the catalyst oxides (CuO, PdO, and CeO_2). At low temperatures, CO adsorbs onto favorable available sites likely associated with the transition metal and eventually reacts with surface O to form 'excess' CO_2 which is not accompanied by simultaneous H_2 production as indicated in Fig. 5. This suggests that the oxidation is driven by a reduction in surface O associated with the metal or neighboring ceria lattice.

The shapes of the low-temperature CO_2 peaks may indicate relationships between catalyst structure and function since peaks at different temperatures have been identified to O sites with different reduction enthalpies [13]. Thus, the CO_2 peak shapes were used to investigate the roles of the Pd and Cu by comparing the bimetallic Pd/Cu catalysts to those with only Pd or only Cu. Fig. 6 shows low-temperature CO_2 production during TPSR (in 5% CO, 10% H_2O, and balance Ar) as a function of temperature for ceria-based fibers with only 2 wt% Pd incorporation, with only 10 wt% Cu incorporation, and with 2/10 wt% Pd/Cu. For the Cu-containing catalysts in Fig. 6, copper acetate was used as the Cu precursor salt.

For the low temperatures in Fig. 6, a large portion of CO_2 production is due to reduction of Cu and Pd, although other studies have indicated that ceria, particularly in close contact with the transition metals, may participate in the reduction as well, even below 200 °C [45]. This explains why the 2 wt% Pd catalyst, with fewer moles of metal per g of catalyst than the 10 wt% Cu or 2/10 wt% Pd/Cu, has significantly less CO_2 production. Both catalysts containing copper have a low-temperature CO_2 release peak below 100 °C, that is not seen for the Pd-only catalyst. Si et al. assigned this initial CO_2 peak to reduction of highly dispersed CuO on the ceria surface [3]. As temperature increases, a more prominent, main CO_2 production peak appears for all three catalyst compositions between 100 and
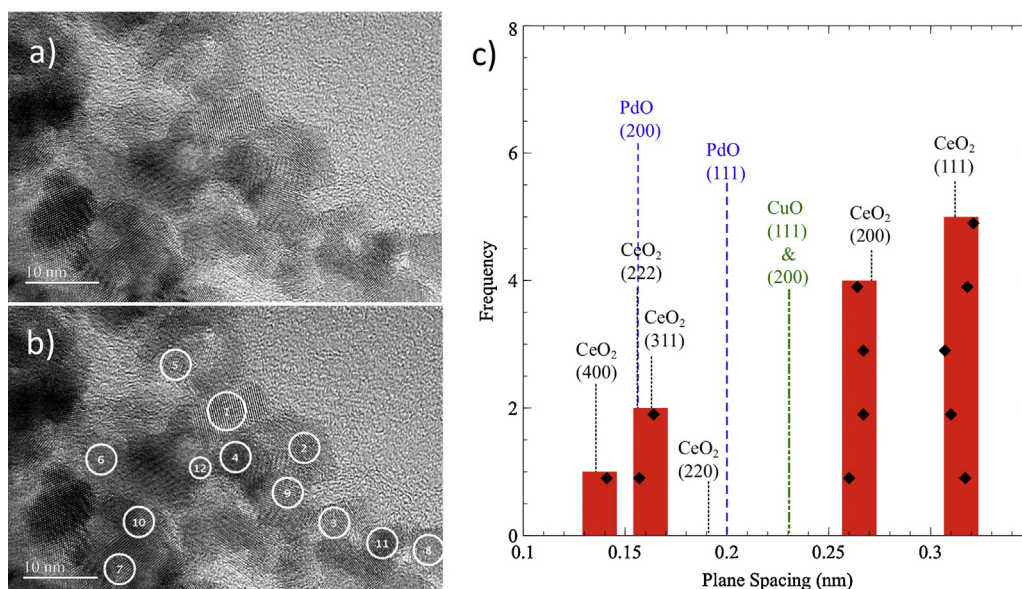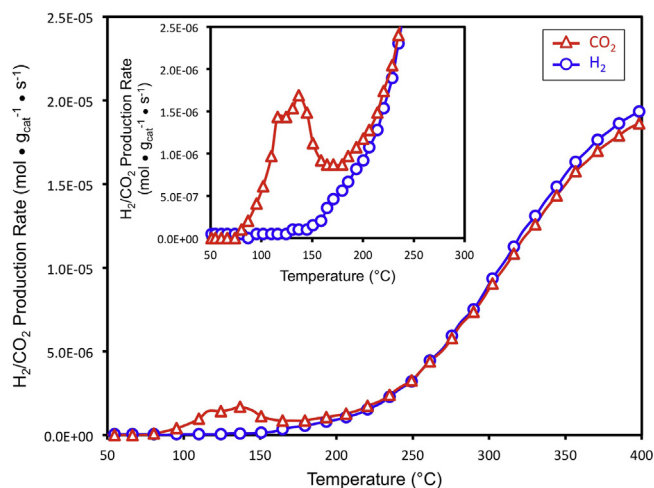
Fig. 4. HRTEM image analysis of the fresh 2/10 wt% Pd/Cu–CeO$_2$ catalyst sample prepared with the (Ac) Cu precursor salt. The base image (a), is shown with selected regions of interest (b), and the measured plane spacings are presented as points and a histogram in (c) along with the plane spacings for CeO$_2$ and the highest intensity planes for PdO and CuO.

Table 2
Total excess CO$_2$ produced by initial peak during temperature ramp at 2 °C min^{-1} under 5% CO, 10% H$_2$O, balance Ar for ceria-based catalyst fibers prepared from copper acetate and/or palladium nitrate precursor salts.

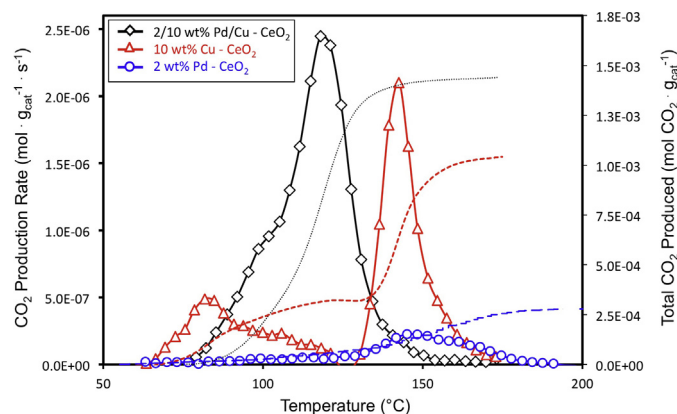| Catalyst	Total CO$_2$ released (mol CO$_2$/g$_{cat}$)	CO$_2$ released per mol Pd + Cu (mol CO$_2$/mol metal)
10 wt% Cu	1.05E−03	0.68
2 wt% Pd	2.75E−04	1.47
2/10 wt% Pd/Cu	1.40E−03	0.82

150 °C. This peak may be associated with the slower reduction of oxide species associated with near surface Cu and/or Pd integrated into the ceria matrix. Interestingly, the integrated values of the total moles of excess CO$_2$ released due to catalyst reduction as plotted in Fig. 6 can be compared to the moles of Pd and/or Cu in the different catalyst. This comparison shown in Table 2 reveals that under the

WGS conditions, the moles of excess CO$_2$ released can account for more than 60% of the Pd + Cu being reduced. Adding the Pd increases the fraction of total metal reduced and for the Pd only catalyst, the excess CO$_2$ production is greater than expected for complete Pd reduction suggesting that some Ce^{4+} near Pd occupied sites may have been reduced at these low temperatures and low effective O$_2$ partial pressure (P_{O_2}) conditions.

The combination of Pd with Cu in the 2/10 wt% Pd/Cu shifts the main CO$_2$ release to lower temperatures. This suggests that the Pd addition enhances low-temperature CO oxidation either by improving CO adsorption and forming of intermediate species and/or by increasing oxygen donation either from the metals or the ceria in the copper-doped ceria matrix. Either effect may provide some explanation for why the Pd/Cu in ceria has significantly higher activity in the time-on-stream tests as illustrated in Fig. 7, which compares CO conversion at the same GHSV of 16,000 h^{-1} for the three catalysts at 400 °C under the same feed conditions (5% CO, 10% H$_2$O, balance Ar). Fig. 7 shows that the Pd/Cu initially provides near equilibrium CO conversion (86% at 400 °C) although the loss of

Fig. 5. CO$_2$ and H$_2$ production rates during TPSR ramp from 50 to 400 °C at 2 °C min^{-1} (in 5% CO, 10% H$_2$O, balance Ar) ceria-based electrospun fiber catalysts with 2/10 wt% PdCu. All tests were done at a GHSV of 16,000 h^{-1}.

Fig. 6. Excess CO$_2$ produced during TPSR ramp from 50 to 400 °C at 2 °C min^{-1} (in 5% CO, 10% H$_2$O, balance Ar) for ceria-based electrospun fiber catalysts (2 wt% Pd, 10 wt% Cu, 2/10 wt% PdCu). All tests were done at a GHSV of 16,000 h^{-1}.
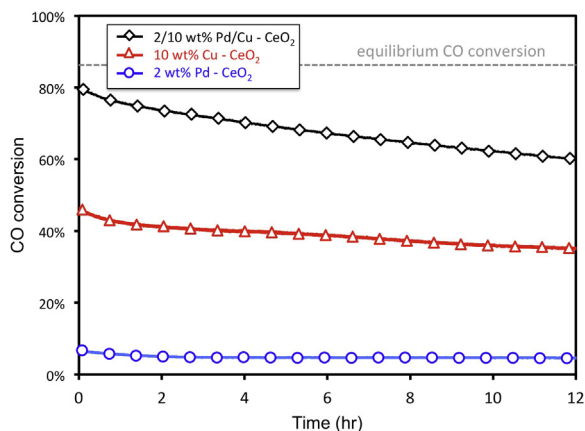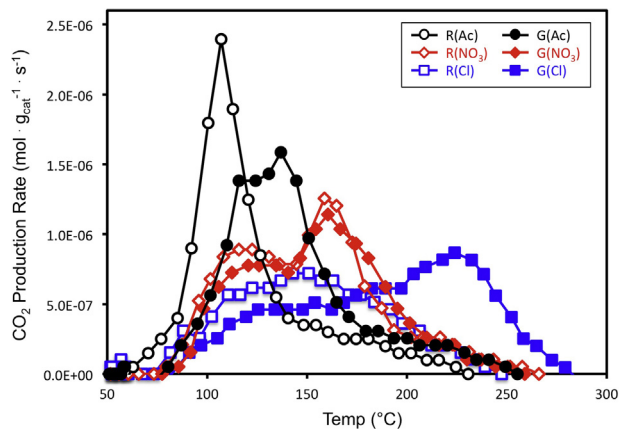
Fig. 7. CO conversion for mono and bi-metallic ceria-based electrospun fiber catalysts (2 wt% Pd, 10 wt% Cu, 2/10 wt% PdCu) during time-on stream test at 400 °C (in 5% CO, 10% H_2O, balance Ar) over 12 h. All tests were done at a GHSV of 16,000 h^{-1}.

Fig. 9. WGS stability tests at 400 °C (in 5% CO, 10% H_2O, balance Ar) and a GHSV of 16,000 h^{-1} for all electrospun ceria-based fibers with 2/10 wt% Pd/Cu shown in Fig. 7. WGS activity for samples is compared to pure ceria electrospun-fibers, which show limited activity.
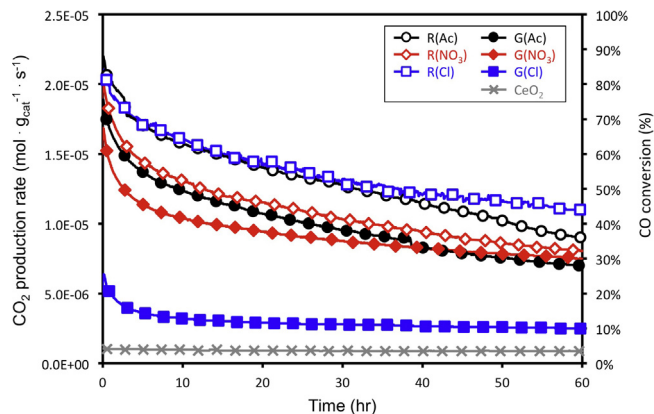
activity that corresponds with Cu segregation and reduction during time-on-stream lowers the CO conversion to around 60% after 12 h of testing.

3.3. Role of copper precursor

The differences observed in the XRD patterns before and after catalyst testing for different Cu precursor salts can be correlated to some degree with catalyst performance. To this end, it is fruitful to compare how the different Cu precursors and calcining process impact the low-temperature excess CO_2 production during TPSR, which is plotted in Fig. 8 for a set of R(X) and G(X) 2/10 wt% Pd/Cu catalyst samples. From Fig. 8, the samples with a copper acetate precursor (both R(Ac) and G(Ac)) show the earliest onset of CO_2 production with peak production between 105 and 140 °C. This correlates with the notion that the catalysts from the acetate precursors have highly-dispersed CuO (as suggested by the XRD), which is most readily reduced. The nitrate-based samples show CO_2 production with two very distinct peaks at 110 and 160 °C, which may be related to dispersed CuO and reduction of the Cu and Pd in the ceria matrix [13]. The G(Cl) sample whose XRD indicated relatively large segregated CuO crystallites has the latest onset of CO_2 reduction with rather broad peaks. As

stated earlier, this catalyst also showed significantly lower activity suggesting that large segregated CuO crystallites are not good for WGS activity.

Integration of the total CO_2 produced during this initial ramp for the acetate and nitrate samples gives a consistent total CO_2 production per g of catalyst (to within ±0.1 mmol per g of catalyst). This is true for both the samples treated with the rapid and gentle calcinations. Thus, while the macroscopic fiber structure is strongly affected by the polymer removal step, the accessible metal for activity is not significantly impacted.

The chloride-based samples show lower peak rates of CO_2 production. The G(Cl) sample subjected shows a peak production shifted to ∼230 °C, which may be related to the fact that a significant amount of the Cu is bound up in large domains of relatively pure CuO as indicated in the XRD in Fig. 3b. Although there is limited evidence as discussed later in the XPS results, this may also be related to the presence of Cl on the surface, which may inhibit CO adsorption and/or oxygen donation for CO_2 production. The likely incomplete removal of chloride anions during the gentle polymer removal/calcination clearly has a significant impact on the catalyst behavior/performance.

After the initial TPSR heating, the catalyst sample temperature was maintained at 400 °C and WGS activity as a function of time on stream was measured with the feed mixture described previously (5% CO, 10% H_2O, balance Ar). The mixture flow rate was held at 40 standard cm^3 min^{-1} for an approximate catalyst space velocity of 16,000 h^{-1}. The relatively high space velocity allows for clearer observation of changes in catalyst kinetics with the activity measurements. The time-on-stream activity results, typified in Fig. 9, always showed decline in activity as a function of time. The activity is measured in CO_2 production rate per gram of catalyst, which for these steady feed conditions agrees very well with the H_2 production rate. The initial activity for the different samples followed the trend: G(Cl) ≪ G(NO₃) ≈ G(Ac) ≈ R(NO₃) < R(Ac) ≈ R(Cl). This order was largely maintained as the activity declined over the first 60 h on stream as indicated in Fig. 9. The decay with exposure to the WGS mixture is consistent for all samples, but in each case, activity can be largely restored through an intermittent re-oxidizing of the catalyst by first purging the reactor with Ar, then flowing 2% O_2 in Ar into the reactor for 30 min at 400 °C before purging the reactor with Ar and then restoring the original feed mixture.

Explanations for the loss of activity during time-on-stream testing for ceria-based catalysts have included the build-up of stable carbon-containing species (formates [25] or carbonates [2]) or the

Fig. 8. Excess CO_2 produced during TPSR ramp from 50 to 400 °C at 2 °C min^{-1} (in 5% CO, 10% H_2O, balance Ar) at a GHSV of 16,000 h^{-1} for electrospun ceria-based fibers with 2/10 wt% Pd/Cu synthesized with different Cu precursor salts and different calcining processes.

loss of surface vacancies for adsorbing and splitting H_2O to drive the necessary redox process [52]. For our tests, upon reoxidation with 2% O_2 for reactivation, no CO_2 release was detected suggesting that the surface was not blocked by formates or carbonates. Thus, although adsorbed formates and carbonates have been observed on metal-supported ceria catalysts and implicated in the rate-limiting step for WGS at relatively low temperatures, their reduced stability at high temperature may explain why their was no evidence of a significant build-up of carbon-containing adsorbates on the surface at 400 °C that is driving the oxidation. As discussed below, there is some evidence that the increased metal reduction and segregation during WGS exposure at 400 °C reduces the availability of strong metal–ceria interactions that provides increased vacancies for H_2O adsorption and H_2 formation [3,28].

The importance of available O for sustaining WGS activity explains why several authors have explored O_2-assisted WGS with similar catalyst systems [31,44,45]. The mechanism for inhibiting the availability of O over time in the reducing WGS mixture remains a matter of debate, but further catalyst characterization here does provide some further insight as discussed in Section 4.

Pure ceria fibers (synthesized without adding Cu or Pd precursors) were also tested in an identical manner to the other catalysts, and shown to be slightly active for WGS at 400 °C. Consistent with the ceria-based WGS literature, the activity for the pure ceria is stable but substantially lower than the activity given for the Pd/Cu loaded catalysts as shown in Fig. 9. Combined with the understanding that the ceria with Pd/Cu is partially reduced upon initial exposure to the WGS mixture during catalyst heating, this result
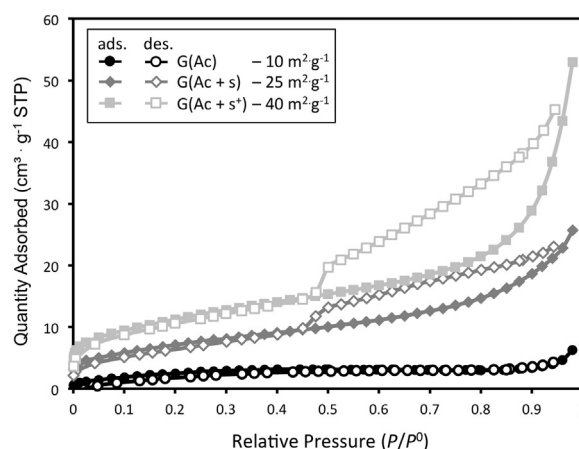

Fig. 10. N_2 adsorption/desorption for tested ceria-based electrospun fiber catalysts with 2/10 wt% Pd/Cu. G(Ac), G(Ac + s), and G(Ac + s+) represent gently calcined samples with copper acetate precursor and varying degrees of surfactant in precursor solution to enhance surface area. Adding surfactant to the spinning solution induced porosity in the fiber materials and increased surface area of the final fiber materials.

indicates that the Pd and Cu interactions with the ceria reduction play a critical role in the high WGS activity and its decay. Shinde and Madras [53,54] have recently captured this three-step mechanism involving O extraction from ceria by the metal for CO oxidation as discussed further in Section 4.
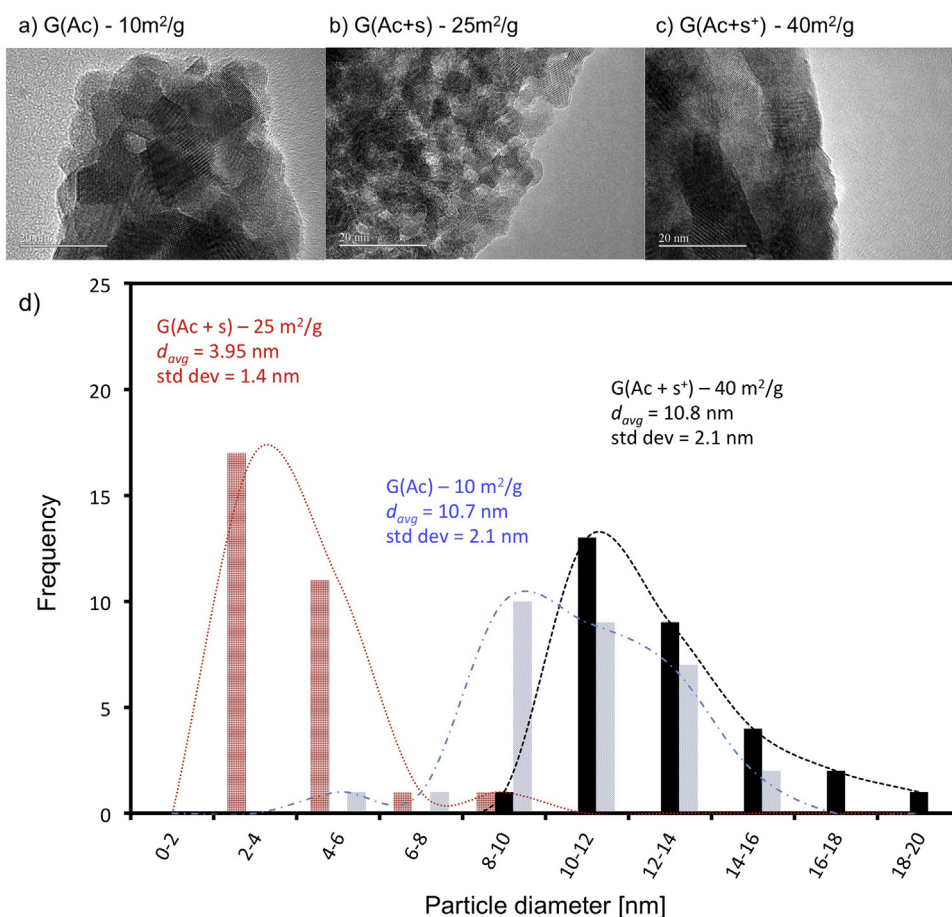
Fig. 11. TEM images of electrospun ceria fibers with 2/10 wt% Pd/Cu after catalytic testing for 60 h at 400 °C and subsequent oxidation in air for 3 h at 450 °C. Individual fiber TEM images for different amounts of surfactant added to precursor solution: (a) G(Ac) with no surfactant, (b) G(Ac + s) with low amount of surfactant, and (c) G(Ac + s+) with a high amount of surfactant. In (d) ceria crystallite diameter distributions based on TEM image analysis are shown for the samples with different surfactant addition.
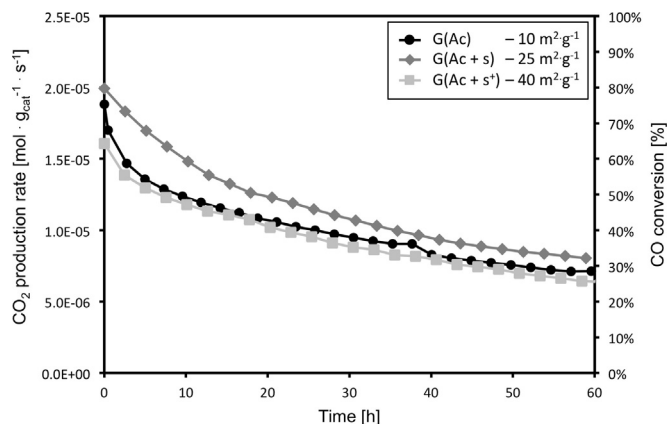
Fig. 12. WGS stability tests at 400 °C (in 5% CO, 10% H_2O, balance Ar) and a GHSV of 16,000 h^{-1} for electrospun ceria fibers with 2/10 wt% Pd/Cu and different amounts of surfactant added to precursor solution: G(Ac) with no surfactant, G(Ac + s) with low amount of surfactant, and G(Ac + s$^+$) with a high amount of surfactant.

3.4. Surface area effects

The importance of available metal sites at the surface of the ceria lattice suggests that increased surface area may impact WGS activity [55]. To explore how increasing fiber surface area might impact fiber catalyst activity, varying amounts of surfactant (Pluronic L-61) were added to the electrospinning solution to lower the surface tension of the solution and thus reduce the diameter of the as-spun fibers. The surfactant also increased fiber porosity via the formation of micelles, which produced voids in the ceramic fiber after the polymer removal step [56,57]. The induced porosity in the fibers is illustrated by the increased total surface area determined from the N_2 adsorption/desorption surface measurements shown in Fig. 10. The G(Ac) sample (with no surfactant added) had a surface area of 10 m^2/g with no evidence of a porous fiber structure. The gently calcined samples with surfactant added – G(Ac + s) for 0.2 g surfactant added to the synthesis solution and G(Ac + s$^+$) for 0.4 g surfactant added – had BET surface areas of 25 and 40 m^2/g respectively as shown in Fig. 10.

The increased porosity at higher surfactant loadings did not however correlate with ceria crystallite size for the sample. As shown in Fig. 11, crystallite size as measured by TEM image analysis of tested catalyst samples indicated that the average ceria crystallite size was lowest for the intermediate surfactant loading, G(Ac + s). The differences in ceria crystallite size, however, only had a minor impact on catalytic activity. Fig. 12 shows activity results for the time-on-stream measurements of the different samples at 400 °C and a GHSV of ~16,000 h^{-1}. Although the activity was highest for the G(Ac + s) sample with the smaller average crystallite size, the difference in CO_2 production rates vary by less than 20% over the entire period of activity decay despite the significant variation in ceria crystallite size. Interestingly, activity did not correlate with total sample surface area suggesting that the rate-controlling processes are not related simply to total ceria surface area.

The rate of activity decay shown in Fig. 12 over the 60 h on stream also did not depend on ceria surface area or average crystallite size. Fiber morphology (surface area) or structure (crystallite size) had limited impact on the catalyst activity and its transient decay. This suggests that the rate-controlling processes are not tied strictly to ceria surface area but to regions of strong metal ceria interactions as claimed in earlier work by Avgoropoulos et al. [28]. These issues are discussed further in next section.

4. Discussion

The present study investigated how electrospinning conditions impacted the transition metal–ceria WGS catalyst morphology, structure, and performance and was not intended to settle the substantive debates in the literature on the kinetic mechanism for WGS on ceria-supported catalysts. Nonetheless, the results and further catalyst characterization provide some rudimentary insight into the WGS reactions on the ceria-supported metals.

Studies on the WGS reaction on ceria-supported metal catalysts have presented seemingly competing mechanisms. The mechanisms can largely be classified as 'redox' and 'associative formate' rate-limited schemes [11,25,26,52–54,58,59]. In both mechanisms, CO adsorption is assumed to occur on a site associated with the metal as in reaction (R2), whether it is supported on the ceria or incorporated into the ceria lattice at the surface [3].

$$CO(gas) + [](metal) \leftrightarrow CO(metal) \qquad (R2)$$
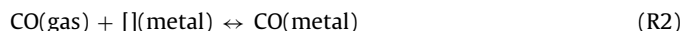
where '[](metal)' represents an unoccupied site associated with the metal, here Cu and/or Pd.

In the redox mechanism, CO absorbed on the metal sites is oxidized by O donated from the neighboring ceria lattice as indicated in Reaction (R3) [52–54].

$$CO(metal) + O(Ce) \leftrightarrow CO_2(gas) + [](metal) + V_O(Ce) \qquad (R3)$$
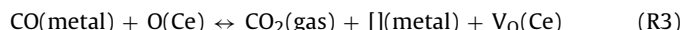
'(Ce)' in reaction (R3) represents an oxide site on the ceria lattice which may have a neighboring metal (Pd or Cu) cation. The resulting vacancy V_O(Ce) provides a site for H_2O adsorption and dissociation as shown in reaction (R4), which completes the WGS reaction (global reaction (R1)).

$$H_2O(gas) + V_O(Ce) \leftrightarrow H_2(gas) + O(Ce) \qquad (R4)$$
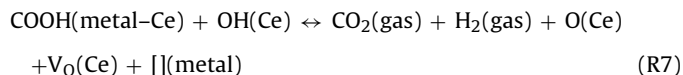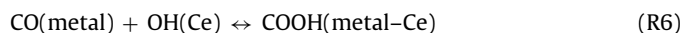
Reaction (R4) is actually a multi-step reaction involving adsorption, O incorporation, surface dissociation, and H_2 desorption. In the reducing water–gas-shift mixture (an effective $P_{O_2} = 1.5 \times 10^{-32}$ bar) of the time-on-stream test conditions of this study, the rate of reaction (R4) is likely controlled by the presence/availability of vacancies for the initial adsorption and O incorporation, which under some conditions may be critical to the overall WGS reaction rate as indicated recently [53,54].

In the associative formate mechanism, H_2O adsorption provides active OH on the ceria surface according to (R5) [24,25,60,61]

$$H_2O(gas) + V_O(Ce) + O(Ce) \leftrightarrow 2OH(Ce) \qquad (R5)$$
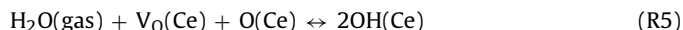
With the adsorbed OH on the ceria, adsorbed CO on neighboring metal sites reacts to form a relatively stable formate (reaction (R6)) that then in a rate-limiting step, decomposes preferably in with the aid of additional OH on the ceria to form CO_2 and H_2 (reaction (R7))

$$CO(metal) + OH(Ce) \leftrightarrow COOH(metal–Ce) \qquad (R6)$$

$$COOH(metal–Ce) + OH(Ce) \leftrightarrow CO_2(gas) + H_2(gas) + O(Ce)$$
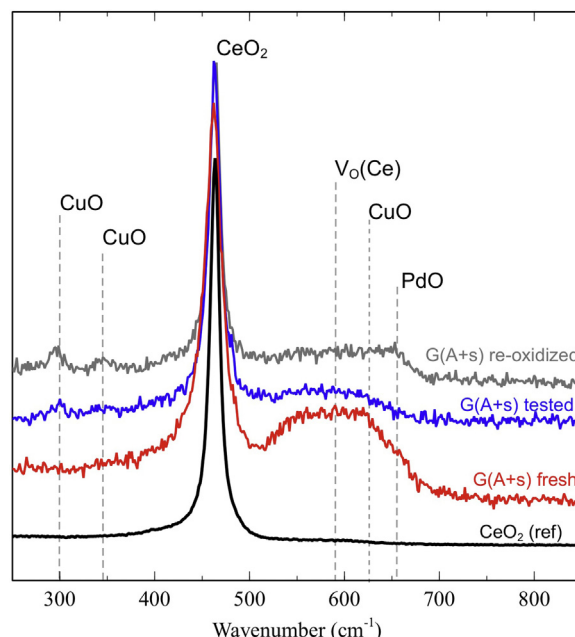$$+V_O(Ce) + [](metal) \qquad (R7)$$

While various studies have presented evidence for both mechanisms, a review of the ceria-based WGS literature suggests that different conditions may favor one mechanism over the other. With relevance to this study, higher temperatures will tend to destabilize the formate and increase oxide mobility in the ceria. As such, higher temperatures (≥300 °C), like in this study, may favor a more direct redox reaction. Previous studies on Ce-based precious metal catalysts at 300 °C and higher with isotopically tagged molecules suggest that the redox mechanism dominates under such conditions similar [52–54].
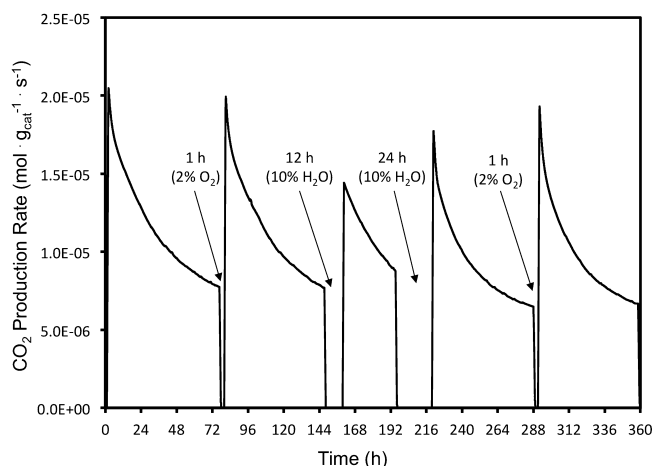
Fig. 13. Time-on-stream activity tests at 400 °C with intermittent re-oxidation with H_2O and O_2 for electrospun ceria fibers with 2/10 wt% Pd/Cu (sample G(Ac + s)). Test conditions are in 5% CO, 10% H_2O, balance Ar at a GHSV of 16,000 h^{-1}. Results show decay of activity with time-on-stream but full activity recovery by flowing 2% O_2 in Ar for 1 h and only partial activity recovery by flowing 10% H_2O for 12 or 24 h.

Fig. 14. Raman spectra from the G(Ac + s) catalyst sample shown in Fig. 12 and CeO_2 fibers for reference. Spectra are shown for the freshly calcined ('fresh'), after testing for 360 h ('tested') with periodic re-oxidation as shown in Fig. 12, and following re-oxidation of the tested sample ('re-oxidized').

In addition to higher temperatures, Cu and/or Pd incorporation into the Ce lattice may also favor a redox mechanism. DFT studies have indicated a decrease the enthalpy of formation for ceria vacancies with divalent cation doping like Pd and Cu [62–64]. Thus, Cu and Pd stabilized in the near-surface lattice may accelerate reaction R3 in the redox mechanism. On the other hand, any loss of Cu and/or Pd from the ceria lattice due to phase segregation as indicated by the XRD in Fig. 3 should increase the energy barrier for vacancy formation and thus R3, which would reduce overall catalyst activity as a function of time-on-stream. Several studies that have shown the formate mechanism to better describe the WGS rate-limiting step tend to be at lower temperatures where the formates are more stable [25,65]. They also focus on ceria-supported metal catalysts from incipient wetness, which tends to produce catalysts with larger surface metals particles and less metal in the CeO_2 lattice than co-precipitation or similar methods.

To explore how these mechanisms may describe the observed catalyst deactivation during time-on-stream testing in this study, a G(Ac + s) sample (2/10 wt% Pd/Cu with added surfactant in the precursor) was operated for 360 h with a series of oxidative treatments with either O_2 or H_2O to restore activity. The re-oxidation treatments were performed at selected intervals after significant activity decay as shown in Fig. 13. The first oxidative treatment was completed by halting the flow of CO and H_2O, purging the reactor with Ar before adding 2 vol% O_2 to the Ar for 1 h, before purging the reactor again and restoring the WGS feed flow. The initial catalyst WGS activity was almost fully restored after the O_2 treatment, and the activity decay followed the same trend as the initial decay. After leaving the system on-stream for 3 days and allowing for a decline in activity, steam was used to restore the catalyst activity by first flowing 10% H_2O in Ar for 12 h, and then 24 h at 400 °C. Steam, which has an effective $P_{O_2} = 1.3 \times 10^{-12}$ bar at 400 °C, only partially restored the catalytic activity through re-oxidation as indicated in Fig. 13. The low P_{O_2} (with H_2O) at 400 °C likely makes the re-oxidation and re-incorporation of any reduced metal species into the ceria lattice relatively slow. Thus, even after 24-h exposure to 0.1 bar H_2O, the ceria–metal catalyst activity was not fully restored as illustrated in Fig. 13. On the other hand, hour-long pulses of O_2 at 0.02 bar fully restored the WGS activity of the ceria–metal catalyst. Thus, the regular decline in activity as a function of time on stream is reversible via oxidative treatments. If the deactivation is primarily due to accumulation of adsorbates, the long-term steam exposure would likely have provided

comparable activity recovery to the O_2 pulse. Furthermore, during the rapid switching from inert (Ar) to oxidizing (0.02 bar O_2 in Ar balance) flows, no CO_2 release was detected. Thus, it is unlikely that the observed deactivation is determined by a surface site blocking via CO_3^{2-} species. Rather, the deactivation is likely related to the accumulation of reduced metals species at the catalyst surface as discussed by Ciston et al. [66] who showed the accumulation of an amorphous CuO surface layer (via environmental TEM and in situ XRD) when a solid solution $Ce_{0.8}Cu_{0.2}O_{2-\delta}$ (similar Ce/Cu molar ratio to the materials in this study) catalyst underwent reduction and oxidation cycles. The authors further demonstrated that the amorphous Cu-rich surface layer can be partially eliminated via an oxidative treatment during which Cu ions re-incorporate into the CeO_2 lattice. This movement of metal ions into and out of near-surface CeO_2 lattice is of increasing interest for the catalyst research community and has been studied in some depth for solid solutions of CeO_2 and Pd, Cu, and Pt in particular, though interest in other divalent transition metals is growing [31,64,67,68].

While both mechanisms provide a basis for explaining the decay in activity with time-on-stream, the reoxidation and reactivation of the catalyst by oxidation with O_2 or H_2O showed no evidence of carbon-containing species on the surface. This suggests minimal presence of formates or similar intermediates blocking adsorption sites at our test conditions. On the other hand, the relatively slow time-scales of the activity decay with the time-on-stream tests suggest a slower bulk-mediated process that drops vacancy availability on the ceria surface. A loss in the availability of surface vacancies can be caused by multiple mechanisms: loss of energetically favorable sites due to phase segregation of transition metals and/or physical blocking of ceria by phase-segregated metal/metal oxides.

To explore this hypothesis further, ex situ Raman characterization of fresh, tested, and reoxidized catalyst (G(Ac + s)) were employed with results presented in Fig. 14. Key features of Raman spectroscopy of ceria-based materials are first the primary peak at 462 cm^{-1} attributed to the CeO_2 lattice F_{2g} mode, and a broader secondary peak centered at approximately 590 cm^{-1} related to the concentration of oxygen vacancies in the fluorite lattice. The

strong secondary peak in the fresh samples demonstrates that the Pd and Cu are at least partially substituted into the CeO_2 lattice, and that charge-compensating oxygen vacancies (stable in air) are formed as a result [69–71]. The vacancy peak is weakened after 60 h of WGS testing, and this reduction in vacancies corresponds to evidence of some surface segregation of Cu and Pd as indicated in the XRD in Fig. 3. Thus, while some fraction of the metals segregate at the surface during the WGS testing at 400 °C, some fraction of Cu and Pd remains incorporated into the ceria lattice. The appearance of small peaks attributed to near surface CuO (distinct peaks ca. 300 and 350 cm^{-1} in Fig. 14) and additional shoulders of the defect peak attributed to surface CuO and PdO (ca. 625 and 650 cm^{-1} respectively) accompanied the weakening of the vacancy peak and suggested that the concentration of incorporated Cu and Pd decreased due to surface segregation. Due to the ex situ nature of the Raman measurements and exposure to ambient air following sample removal from the reactor, the in situ oxidation state of the segregated surface metal species is not clear, but recent in situ XPS studies at a synchrotron indicate that they are likely reduced before exposure to air [72].

Re-oxidation of the catalyst in 2% O_2, which restores activity as shown in Fig. 13 with this same sample, results in an increase in the intensity of both the CuO and PdO peaks. Even though the catalyst is reactivated with re-oxidation, the ex situ Raman spectra suggests that it may not be due to a restoration of original vacancy concentrations (i.e., full Pd and Cu re-incorporation into the lattice). However, the formation of the small domains of PdO and CuO during reoxidation may lead to interesting dynamics between the ceria and the metal species during reduction of the metal oxides upon re-exposure to the reducing WGS environment. These dynamics require careful in situ Raman and/or XPS measurements that can provide improved understanding, not only of the reactivation process but also of the nature of the metal–ceria interactions that promote highest activity. Some recent, relevant in situ work probing the oxidation state of ceria-based WGS catalyst provides some insight into the dynamic nature of the metals under oxidizing and reducing conditions as well as their interactions with the CeO_2 lattice. [14,45,66,73–76] Those studies demonstrated that formation of solid solution type species (e.g., Ce^{4+}–[]–Pd^{2+}–O–Ce^{4+}, Ce^{4+}–[]–Cu^{2+}–O–Ce^{4+}, with the 2^+ metals) creates oxide vacancies and enhances catalyst performance for many important reactions including WGS [44,45,73,77,78]. Gulyaev and co-workers demonstrated that an oxidizing environment enhances formation of Ce^{4+}–[]–Pd^{2+}–O–Ce^{4+} in Pd-impregnated ceria catalysts [68], which appear critical to catalyst activity. The dynamic nature of the metal species under the reducing environment of WGS reactants indicates the importance of observing the catalyst surface with surface-sensitive XPS measurements.

To that end, a G(Ac + s) sample (2/10 wt% Pd/Cu with added surfactant in the precursor) was studied via XPS in conjunction with the 360 h time-on-stream test. XPS measurements were taken at three different conditions: (1) 'fresh' – unexposed to WGS reaction conditions, (2) 'tested' – quenched in Ar after a 360 h test at 400 °C, and (3) 're-oxidized' – tested sample heated in air to 450 °C for 3 h. After quenching in Ar, exposure to air was minimized for the spent sample, but by nature of the ex situ characterization, the sample was exposed to the ambient environment under which Ce^{3+} to Ce^{4+} oxidation is known to occur. Indeed, reduced Ce^{3+} was not observed during examination of the Ce 3d spectra. Surface oxidation states of the Cu and Pd metals were explored with the Cu 2p$_{3/2}$ as presented in Fig. 15a and the Pd 3d$_{3/2}$ and 3d$_{5/2}$ spectra as presented in Fig. 15b.

The Cu 2p$_{3/2}$ spectra shown in Fig. 15a presents a challenge for interpretation because of the overlapping peaks of various Cu species in the binding energy (BE) range between 932 and 933 eV. XPS analysis of bimetallic Pd/Cu–CeO_2 catalysts by Fox

Table 3
Ratios of copper and palladium to cerium at the surface for the 2% Pd/10% Cu on ceria prepared with copper acetate precursors.

	Cu/Ce	Pd/Ce	(Cu + Pd)/Ce
Fresh	0.257	0.021	0.278
Tested	0.509	0.015	0.524
Re-oxidized	0.307	0.013	0.320

et al. discussed the presence of overlapping peaks for metallic Cu^0, Cu_2O, and Cu_2O in this range and the dynamic behavior and mobility of Cu^0, Cu_2O, CuO and Cu^{x+}_{Ce} under oxidizing/reducing conditions [45,55,79]. This last species Cu^{x+}_{Ce} represents Cu incorporated in the ceria exposed to reducing conditions with an oxidation state likely close to 2+. It is not possible to differentiate between Cu^0/Cu_2O and CuO/Cu^{x+}_{Ce} within the Cu 2p$_{3/2}$ spectrum, As such, the Cu XPS must be considered along with the other characterization methods to more fully elucidate the nature of the Cu ions in these catalyst samples. To further complicate interpretation of the XPS data, the samples were exposed to air (at ambient temperature) before XPS analysis, and thus, surface Cu species are likely to be oxidized as confirmed by the Raman spectra in Fig. 14. An increase in the intensity of the peak assigned to CuO/Cu^{x+}_{Ce} upon testing and associated catalyst reduction offers further support of increased Cu surface concentration during testing, but the Cu occupies a predominantly 2+ state on the surface due to the strongly oxophilic nature of Cu. Interestingly, Fig. 15a shows that re-oxidation at 450 °C does not return the Cu^0/Cu_2O peak to fresh conditions even though re-oxidation does recover activity. Instead, the relative peak strength grows further with re-oxidation. A possible explanation for the growth in relative strength is the reincorporation of surface CuO into the ceria lattice for the relatively high temperature oxidation.

While the Cu 2p$_{3/2}$ spectrum is difficult to interpret, the Pd 3d spectra shown in Fig. 15b provides a relatively clear picture of the behavior of Pd on the surface. The Pd 3d$_{3/2}$ and 3d$_{5/2}$ BE spectra for the untested sample demonstrate the presence of distinct Pd oxide species, as well as Pd–CeO_2 solid solution species. For the untested sample, no Pd metal (Pd^0) is present. The last exposure environment for the untested catalyst was 550 °C in air, which is expected to produce oxidized Pd [80]. Following the WGS testing at 400 °C, reduced Pd metal (Pd^0) on the catalyst surface appears strongly as demonstrated by the BE peaks at 335.6 and 341.0 eV, which were previously absent in the 'fresh' sample. Upon re-oxidation, the Pd metal peaks are no longer present, and the BE spectra of the 're-oxidized' catalyst shows that most of the re-oxidized Pd appears as dispersed combination PdO with a smaller fraction being reincorporated into the CeO_2 lattice (Pd^{2+}_{Ce}) [45,78]. Comparing the relative peak intensities for PdO and Pd^{2+}_{Ce} as a function of conditions, it is clear that the fresh catalyst shows a ratio of Pd^{2+}_{Ce}/PdO greater than 1. The tested sample maintains this ratio, indicating that the surface Pd^0 comes from both the surface PdO as well as the Pd^{2+}_{Ce} species. Upon re-oxidation, the Pd^{2+}_{Ce}/PdO peak intensity ratio is less than 1, indicating that incorporation of Pd into the CeO_2 lattice after re-oxidation is less than in the 'fresh' catalyst state.

These results are consistent with the growing body of literature concerning the mobility of metal ions in the CeO_2 lattice for solid-solution systems, though these phenomena are still not well understood. The integrated area of the Pd 3d and Cu 2p peaks relative to the Ce 3d peaks (not shown in Fig. 15) provide a basis for assessing the relative fraction of Pd and Cu on the surface. Table 3 shows the ratio of Cu to Ce and Pd to Ce from the surface-sensitive XPS measurements. The results show that in particular for Cu, reduction after 60 h of WGS testing at 400 °C almost doubles the amount of Cu at the surface from the fresh catalyst state. Interestingly, reoxidation reduces the fraction of Cu measurable
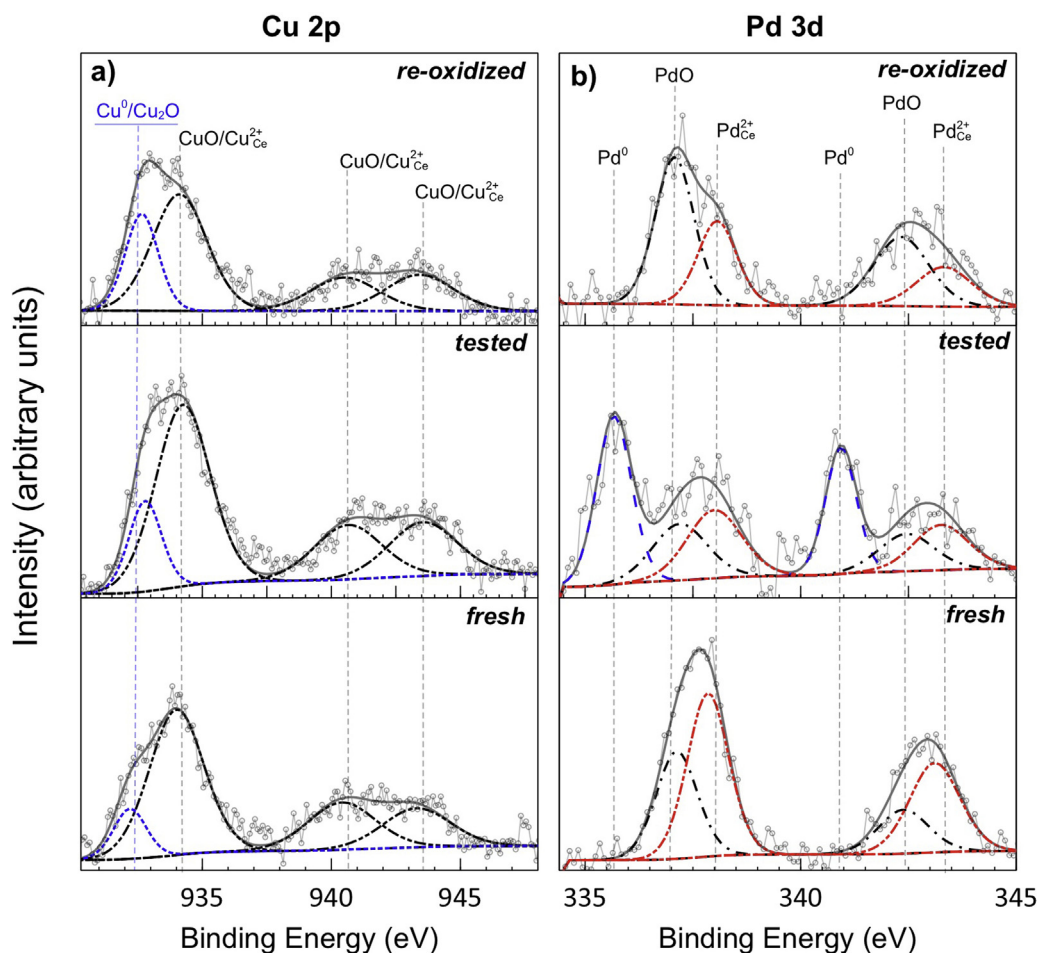
Fig. 15. X-ray photoelectron spectra before ('fresh') and after ('tested') testing as WGS catalysts for 60 h at 400 °C and after exposure (re-oxidized) for 3 h in air at 450 °C for (a) Pd 3d peaks and (b) Cu $2p_{3/2}$ peaks.

by XPS suggesting that some of the Cu is either lost due to CuO agglomeration or re-incorporation into the ceria lattice. The Raman measurements in Fig. 14 suggests that there is some degree of CuO agglomeration, but the full recovery of the catalyst suggest that highly active Cu and Pd species are created near the surface. Further in situ XPS measurements of re-oxidation and reduction in WGS environments will provide valuable insight as to the degree of Cu and Pd reincorporation during reoxidation/reactivation of the these catalysts.

Overall, the ex situ XPS measurements here provides glimpses into the dynamic nature of the Pd/Cu ceria-based catalyst structure, but more extensive studies with broader array of characterization techniques are needed to provide a fuller mechanistic understanding of how the Cu and Pd structure and oxidation states impact activity. This study, in line with previous studies on Pd/Cu ceria-based catalysts, shows how the dynamic nature of the catalyst nanocrystalline structure and surface under reactive conditions correlates with changes in catalyst activity, in particular slow WGS deactivation under reducing conditions and activity recovery with high-temperature re-oxidation. In addition, this study has shown that such dynamic nanocrystalline structures can be attained with a relatively straightforward catalyst synthesis technique based on single-pot.

5. Conclusions

In this study, electrospinning has been used to produce nano-crystalline fibrous structures of Pd, Cu, and Pd/Cu ceria-based

catalysts for WGS. With 'gentle' oxidative removal of the electro-spun polymer material, the resulting ceria-based catalysts formed a non-woven mat consisting of nano-fibers (<200 nm in diameter) and individual ceria crystallites (<15 nm in diameter). Characterization via XRD, Raman spectroscopy, and XPS of untested 2/10 wt% Pd/Cu ceria-based fibers indicated the presence of solid solutions, with varying amounts of phase-segregated CuO depending on the Cu precursor salt (with non-preferable chlorides showing increased segregation).

60+ hours of time-on-stream testing of all catalysts in the WGS environment (5% CO, 10% H_2O, balance Ar) at 400 °C resulted in asymptotic decay of catalyst activity which coincided with an increased presence of Cu species at the catalyst surface as measured by Raman and XPS. XPS measurements suggested a significant presence of reduced Cu and Pd at the surface after WGS reactions. The loss of WGS activity was largely recovered by exposure to an oxidizing environment with O_2 providing much more effective recovery than H_2O. XPS analysis and Raman spectra of reoxidized catalyst indicated that the recovered activity corresponds to re-oxidation of surface Pd largely to PdO without any evidence of PdO particles, suggesting that Pd may have been in large part reincorporated into the ceria. The segregated Cu species do appear to form some CuO surface phases, but the amount of Cu on the surface decreases with reoxidation, which suggests that some surface Cu may have also been reincorporated into the ceria lattice. The link between catalyst activity and the transition metals incorporated into the ceria lattice may be tied to metals facilitating low-energy barriers to O vacancy formation in the ceria lattice and thereby promoting H_2O

splitting on the ceria surface. Pd and Cu metal reduction and surface segregation during WGS testing conditions may reduce the favorable sites in the ceria lattice for vacancy formation, which provides an explanation for the slow deactivation. While further detailed studies are needed to confirm this, this hypothesis is consistent with the observations presented in this study.

While this study provides only partial insight into the complex mechanism for WGS activity on Pd/Cu ceria catalysts, the study does show that with careful control of relatively simple catalyst preparation methods as electrospinning, highly active catalysts with dynamic structures can be produced. Through continued exploration, such a synthesis method may be optimized to produce high-performance, cost-effective nano-crystalline ceria catalysts. With continued fundamental investigations into understanding the dynamic nature of the transition metals in and on the nano-crystalline ceria structure, hopefully methods for stabilizing the compositional structure and long-term activity can be realized to formulate stable high-activity catalysts for WGS reactors across several critical energy-conversion applications.

Acknowledgements

References

[1] A. Faur Ghenciu, Curr. Opin. Solid State Mater. Sci. 6 (2002) 389–399.
[2] S. Hilaire, X. Wang, T. Luo, R.J. Gorte, J. Wagner, Appl. Catal. A: Gen. 258 (2004) 271–276.
[3] R. Si, J. Raitano, N. Yi, L.H. Zhang, S.W. Chan, M. Flytzani-Stephanopoulos, Catal. Today 180 (2012) 68–80.
[4] C. Song, Catal. Today 77 (2002) 17–49.
[5] W. Ruettinger, O. Ilinich, R.J. Farrauto, J. Power Sources 118 (2003) 61–65.
[6] X. Wang, R.J. Gorte, J.P. Wagner, J. Catal. 212 (2002) 225–230.
[7] X. Wang, R.J. Gorte, Appl. Catal. A: Gen. 247 (2003) 157–162.
[8] N.L. Wieder, M. Cargnello, K. Bakhmutsky, T. Montini, P. Fornasiero, R.J. Gorte, J. Phys. Chem. C 115 (2011) 915–919.
[9] W.L. Deng, C. Carpenter, N. Yi, M. Flytzani-Stephanopoulos, Top. Catal. 44 (2007) 199–208.
[10] Q. Fu, H. Saltsburg, M. Flytzani-Stephanopoulos, Science 301 (2003) 935–938.
[11] K. Li, Q. Fu, M. Flytzani-Slephanopoulos, Appl. Catal. B: Environ. 27 (2000) 179–191.
[12] D. Pierre, W.L. Deng, M. Flytzani-Stephanopoulos, Top. Catal. 46 (2007) 363–373.
[13] R. Si, J. Raitano, N. Yi, L. Zhang, S.-W. Chan, M. Flytzani-Stephanopoulos, Catal. Today 180 (2012) 68–80.
[14] L. Barrio, M. Estrella, G. Zhou, W. Wen, J.C. Hanson, A.B. Hungria, A. Hornes, M. Fernandez-Garcia, A. Martinez-Arias, J.A. Rodriguez, J. Phys. Chem. C 114 (2010) 3580–3587.
[15] T. Bunluesin, R.J. Gorte, G.W. Graham, Appl. Catal. B: Environ. 15 (1998) 107–114.
[16] R. Burch, Phys. Chem. Chem. Phys. 8 (2006) 5483–5500.
[17] K. Chayakul, T. Srithanratana, S. Hengrasmee, Catal. Today 175 (2011) 420–429.
[18] K. Chayakul, T. Srithanratana, S. Hengrasmee, J. Mol. Catal. A: Chem. 340 (2011) 39–47.
[19] A.M. Duarte de Farias, P. Bargiela, M.d.G.C. Rocha, M.A. Fraga, J. Catal. 260 (2008) 93–102.
[20] A.M. Duarte de Farias, D. Nguyen-Thanh, M.A. Fraga, Appl. Catal. B: Environ. 93 (2010) 250–258.
[21] R.J. Gorte, AIChE J. 56 (2010) 1126–1135.
[22] S. Hilaire, X. Wang, T. Luo, R.J. Gorte, J. Wagner, Appl. Catal. A: Gen. 215 (2001) 271–278.
[23] S. Pradhan, A.S. Reddy, R.N. Devi, S. Chilukuri, Catal. Today 141 (2009) 72–76.
[24] K.G. Azzam, I.V. Babich, K. Seshan, L. Lefferts, J. Catal. 251 (2007) 153–162.
[25] G. Jacobs, E. Chenu, P.M. Patterson, L. Williams, D. Sparks, G. Thomas, B.H. Davis, Appl. Catal. A: Gen. 258 (2004) 203–214.
[26] H. Sakurai, T. Akita, S. Tsubota, M. Kiuchi, M. Haruta, Appl. Catal. A: Gen. 291 (2005) 179–187.
[27] X.Q. Wang, J.A. Rodriguez, J.C. Hanson, D. Gamarra, A. Martinez-Arias, M. Fernandez-Garcia, J. Phys. Chem. B 110 (2006) 428–434.
[28] G. Avgouropoulos, T. Ioannides, H. Matralis, Appl. Catal. B: Environ. 56 (2005) 87–93.
[29] V. Sharma, P.A. Crozier, R. Sharma, J.B. Adams, Catal. Today 180 (2012) 2–8.
[30] G.N. Vayssilov, Y. Lykhach, A. Migani, T. Staudt, G.P. Petrova, N. Tsud, T. Skála, A. Bruix, F. Illas, K.C. Prince, V.R. Matolín, K.M. Neyman, J. Libuda, Nat. Mater. 10 (2011) 310–315.
[31] M. Kurnatowska, L. Kepinski, W. Mista, Appl. Catal. B: Environ. 117–118 (2012) 135–147.
[32] P.V.D.S. Gunawardana, H.C. Lee, D.H. Kim, Int. J. Hydrogen Energy 34 (2009) 1336–1341.
[33] P. Djinovic, J. Batista, A. Pintar, Appl. Catal. A: Gen. 347 (2008) 23–33.
[34] L. Li, L. Song, H. Wang, C. Chen, Y. She, Y. Zhan, X. Lin, Q. Zheng, Int. J. Hydrogen Energy 36 (2011) 8839–8849.
[35] A.K. Alves, F.A. Berutti, F. Clemens, T. Graule, C.P. Bergmann, Rev. Adv. Mater. Sci. 21 (2009) 200–204.
[36] A.-M. Azad, T. Matthews, J. Swary, Mater. Sci. Eng. B 123 (2005) 252–258.
[37] F.A. Berutti, A.K. Alves, C.P. Bergmann, F.J. Clemens, T. Graule, Particulate Sci. Technol. 27 (2009) 203–209.
[38] F.R. Lamastra, A. Bianco, A. Meriggi, G. Montesperelli, F. Nanni, G. Gusmano, Chem. Eng. J. 145 (2008) 169–175.
[39] V. Thavasi, G. Singh, S. Ramakrishna, Energy Environ. Sci. 1 (2008) 205–221.
[40] P. Viswanathamurthi, N. Bhattarai, C.K. Kim, H.Y. Kim, D.R. Lee, Inorg. Chem. Commun. 7 (2004) 679–682.
[41] Y. Zhang, J. Li, Q. Li, L. Zhu, X. Liu, X. Zhong, J. Meng, X. Cao, J. Colloid Interface Sci. 307 (2007) 567–571.
[42] G.C. Pontelli, R.P. Reolon, A.K. Alves, F.A. Berutti, C.P. Bergmann, Appl. Catal. A: Gen. 405 (2011) 79–83.
[43] H. Tang, H. Sun, D. Chen, X. Jiao, Mater. Lett. 77 (2012) 7–9.
[44] J. Kugai, J.T. Miller, N. Guo, C. Song, J. Catal. 277 (2011) 46–53.
[45] E.B. Fox, A.F. Lee, K. Wilson, C. Song, Top. Catal. 49 (2008) 89–96.
[46] R. Ruiz-Rosas, J. Bedia, J.M. Rosas, M. Lallave, I.G. Loscertales, J. Rodríguez-Mirasol, T. Cordero, Catal. Today 187 (2012) 77–87.
[47] H. Kim, Y. Choi, N. Kanuka, H. Kinoshita, T. Nishiyama, T. Usami, Appl. Catal. A: Gen. 352 (2009) 265–270.
[48] X. Yang, C. Shao, Y. Liu, R. Mu, H. Guan, Thin Solid Films 478 (2005) 228–231.
[49] Q. Cui, X. Dong, J. Wang, M. Li, J. Rare Earths 26 (2008) 664–669.
[50] H. Kang, Y. Zhu, X. Yang, Y. Jing, A. Lengalova, C. Li, J. Colloid Interface Sci. 341 (2010) 303–310.
[51] S.T. Aruna, A.S. Mukasyan, Curr. Opin. Solid State Mater. Sci. 12 (2008) 44–50.
[52] C.M. Kalamaras, S. Americanou, A.M. Efstathiou, J. Catal. 279 (2011) 287–300.
[53] V.M. Shinde, G. Madras, Appl. Catal. B: Environ. 123 (2012) 367–378.
[54] V.M. Shinde, G. Madras, Appl. Catal. B: Environ. 132 (2013) 28–38.
[55] J. Kugai, E.B. Fox, C. Song, Appl. Catal. A: Gen. 456 (2013) 204–214.
[56] S. Madhugiri, B. Sun, P.G. Smirniotis, J.P. Ferraris, K.J. Balkus, Microporous Mesoporous Mater. 69 (2004) 77–83.
[57] Y. Zhao, H. Wang, X. Lu, X. Li, Y. Yang, C. Wang, Mater. Lett. 62 (2008) 143–146.
[58] C.M. Kalamaras, I.D. Gonzalez, R.M. Navarro, J.L.G. Fierro, A.M. Efstathiou, J. Phys. Chem. C 115 (2011) 11595–11610.
[59] C.I. Vignatti, M.S. Avila, C.R. Apesteguia, T.F. Garetto, Catal. Today 171 (2011) 297–303.
[60] T. Shido, Y. Iwasawa, J. Catal. 141 (1993) 71–81.
[61] L.Z. Linganiso, V.R.R. Pendyala, G. Jacobs, B.H. Davis, D.C. Cronauer, A.J. Kropf, C.L. Marshall, Catal. Lett. 141 (2011) 1723–1731.
[62] Z. Lu, Z. Yang, B. He, C. Castleton, K. Hermansson, Chem. Phys. Lett. 510 (2011) 60–66.
[63] M. Aryanpour, A. Khetan, H. Pitsch, ACS Catal. 3 (2013) 1253–1262.
[64] A.B. Kehoe, D.O. Scanlon, G.W. Watson, Chem. Mater. 23 (2011) 4464–4468.
[65] M.C. Ribeiro, G. Jacobs, L. Linganiso, K.G. Azzam, U.M. Graham, B.H. Davis, ACS Catal. 1 (2011) 1375–1383.
[66] J. Ciston, R. Si, J.A. Rodriguez, J.C. Hanson, A. Martiínez-Arias, M. Fernandez-Garciía, Y. Zhu, J. Phys. Chem. C 115 (2011) 13851–13859.
[67] L.Z. Linganiso, G. Jacobs, K.G. Azzam, U.M. Graham, B.H. Davis, D.C. Cronauer, A.J. Kropf, C.L. Marshall, Appl. Catal. A: Gen. 394 (2011) 105–116.
[68] R.V. Gulyaev, A.I. Stadnichenko, E.M. Slavinskaya, A.S. Ivanova, S.V. Koscheev, A.I. Boronin, Appl. Catal. A: Gen. 439–440 (2012) 41–50.
[69] C.Q. Hu, Q.S. Zhu, L. Chen, R.F. Wu, Mater. Res. Bull. 44 (2009) 2174–2180.
[70] L. Li, Y.Y. Zhan, Q. Zheng, Y.H. Zheng, C.Q. Chen, Y.S. She, X.Y. Lin, K.M. Wei, Catal. Lett. 130 (2009) 532–540.
[71] R.V. Gulyaev, A.I. Stadnichenko, E.M. Slavinskaya, A.S. Ivanova, S.V. Koscheev, A.I. Boronin, Appl. Catal. A: Gen. 439 (2012) 41–50.
[72] E.B. Fox, A.F. Lee, K. Wilson, C.S. Song, Top. Catal. 49 (2008) 89–96.
[73] A. Kubacka, R. Si, P. Michorczyk, A. Martínez-Arias, W. Xu, J.C. Hanson, J.A. Rodriguez, M. Fernández-García, Appl. Catal. B: Environ. 132–133 (2013) 423–432.

[74] J.A. Rodriguez, J.C. Hanson, W. Wen, X. Wang, J.L. Brito, A. Martínez-Arias, M. Fernández-García, Catal. Today 145 (2009) 188–194.

[75] A. Martínez-Arias, D. Gamarra, M. Fernández-García, X.Q. Wang, J.C. Hanson, J.A. Rodriguez, J. Catal. 240 (2006) 1–7.

[76] X. Wang, J.A. Rodriguez, J.C. Hanson, D. Gamarra, A. Martínez-Arias, M. Fernández-García, J. Phys. Chem. B 110 (2005) 428–434.

[77] A.L. Cámara, A. Kubacka, Z. Schay, Z. Koppány, A. Martínez-Arias, J. Power Sources 196 (2011) 4364–4369.

[78] J. Kugai, J.T. Miller, N. Guo, C.S. Song, Appl. Catal. B: Environ. 105 (2011) 306–316.

[79] E.B. Fox, S. Velu, M.H. Engelhard, Y.H. Chin, J.T. Miller, J. Kropf, C.S. Song, J. Catal. 260 (2008) 358–370.

[80] S. Colussi, A. Trovarelli, C. Cristiani, L. Lietti, G. Groppi, Catal. Today 180 (2012) 124–130.